



Published in final edited form as:

J Am Chem Soc. 2015 June 3; 137(21): 6912–6919. doi:10.1021/jacs.5b03370.

Experimental Correlation of Substrate Position with Reaction Outcome in the Aliphatic Halogenase, SyrB2

Ryan J. Martinie^a, Jovan Livada^a, Wei-chen Chang^a, Michael T. Green^a, Carsten Krebs^{a,b}, J. Martin Bollinger Jr.^{a,b}, and Alexey Silakov^{a,*}

^aDepartment of Chemistry, The Pennsylvania State University, University Park, PA, USA

^bDepartment of Biochemistry and Molecular Biology, The Pennsylvania State University, University Park, PA, USA

Abstract

The iron(II)- and 2-(oxo)glutarate-dependent (Fe/2OG) oxygenases catalyze an array of challenging transformations, but how individual members of the enzyme family direct different outcomes is poorly understood. The Fe/2OG halogenase, SyrB2, chlorinates C4 of its native substrate, L-threonine appended to the carrier protein, SyrB1, but hydroxylates C5 of L-norvaline and, to a lesser extent, C4 of L-aminobutyric acid when SyrB1 presents these non-native amino acids. To test the hypothesis that positioning of the targeted carbon dictates the outcome, we defined the positions of these three substrates by measuring hyperfine couplings between substrate deuterium atoms and the stable, EPR-active iron-nitrosyl adduct, a surrogate for reaction intermediates. The Fe-²H distances and N-Fe-²H angles, which vary from 4.2 Å and 85° for threonine to 3.4 Å and 65° for norvaline, rationalize the trends in reactivity. This experimental correlation of position to outcome should aid in judging from structural data on other Fe/2OG enzymes whether they suppress hydroxylation or form hydroxylated intermediates on the pathways to other outcomes.

Introduction

Mononuclear^{1–4} and dinuclear^{1,5,6} non-heme iron enzymes, cytochromes P450,⁷ and radical SAM enzymes^{8,9} activate and functionalize inert C-H bonds with a remarkable degree of specificity and selectivity. Members of the iron- and 2-(oxo)glutarate-dependent (Fe/2OG) oxygenase family catalyze a variety of transformations at unactivated carbon centers, including hydroxylation, desaturation, cyclization, stereoinversion, and halogenation; these reactions play crucial roles in microbial metabolism and biosynthesis,² as well as oxygen and body mass homeostasis,^{10–12} DNA repair,^{13–15} epigenetic inheritance, and control of transcription in humans.^{16–18} The mechanistic strategy employed by this family was first elucidated in the hydroxylases.⁴ These enzymes activate oxygen at their common Fe(II)

Copyright © American Chemical Society.

*Corresponding author: alexey.silakov@gmail.com.

Associated Content

Supporting Information. Field-dependent HYSCORE spectra, simulations, skyline plots, tables of simulation parameters, and descriptive diagrams. This material is available free of charge via the Internet at <http://pubs.acs.org>.

cofactor, which is coordinated by a (His)₂(Glu/Asp)₁ “facial triad” ligand set,^{19,20} to form a high-spin ($S = 2$) Fe(IV)-oxo (ferryl) intermediate.^{21–24} This ferryl unit abstracts a hydrogen atom (H•) from the substrate,²⁵ yielding an Fe(III)-hydroxo/substrate-radical intermediate; this radical then couples with the hydroxo ligand (formally HO•), producing the hydroxylated product and an Fe(II) complex.^{4,26,27} Current understanding of the mechanisms employed by other Fe/2OG oxygenases to direct this potent reactivity to only one of several alternative reaction outcomes (e.g. halogenation, stereoinversion, etc.) is incomplete. A robust understanding of this control is a major unmet challenge and will be required for these systems to be exploited for potential biotechnological applications, including production of new drug compounds.

The Fe/2OG aliphatic halogenases provide an ideal system to study enzymatic discrimination between accessible reactivities. SyrB2 from *Pseudomonas syringae* B301D is the founding member of the Fe/2OG aliphatic halogenases.^{28–31} It catalyzes chlorination of the C4 position of L-threonine appended *via* a thioester linkage to the phosphopantetheine arm of the companion aminoacyl carrier protein, SyrB1 (hereafter, all L-aminoacyl-*S*-SyrB1 substrates are abbreviated by designating only the appended amino acid in boldface type, e.g., **Thr**; Figure 1). In SyrB2, the sequence position that normally provides the carboxylate of the canonical facial triad of protein ligands is occupied by an alanine (Ala118), and the co-substrate, chloride (Cl[−]), occupies the vacated site in the iron coordination sphere.³² Fe/2OG halogenases mechanistically parallel the hydroxylases in that both employ ferryl intermediates as the H•-abstracting species.^{33–35} However, following this step, the reactivities diverge: in the halogenases it is the Cl• ligand, rather than the HO•, that couples with the substrate radical. Thus, halogenases generate the substrate radical in a manner similar to the hydroxylases, but are faced with the more difficult challenge of directing it to chlorination rather than hydroxylation. Efficient H• transfer to the ferryl would seemingly imply proximity to the hydroxo ligand in the subsequent step, and HO•/substrate radical coupling occurs readily in the hydroxylases. Yet, the native substrate of SyrB2, **Thr**, is almost exclusively chlorinated (Figure 1),³⁶ although non-native substrates undergo hydroxylation as well as chlorination. Therefore, SyrB2 represents an intriguing case in which two different reaction outcomes catalyzed by this enzyme family (hydroxylation and halogenation) are observed, making it an ideal system for investigating how the enzymes discriminate between reactivities.

Our previous work showed that the *cis*-chloroferryl complex in SyrB2 reacts more rapidly with SyrB1 presenting L-aminobutyric acid (**Aba**) or L-norvaline (**Nva**) than with **Thr**, suggesting a programmed inefficiency in H• abstraction from the native substrate. Formed with **Nva**, the complex decays 130-fold more rapidly (9.5 s^{-1} at 5 °C) than with **Thr** (0.07 s^{-1}); with **Aba**, the rate is intermediate (0.9 s^{-1}) (Figure 1).³⁶ Selectivity for chlorination is also strongly modulated: **Thr** is almost exclusively chlorinated, **Aba** is chlorinated and hydroxylated at C4 to similar extents, and **Nva** is predominately hydroxylated at the C5 position.³⁶ It was reasoned that the decrease in ferryl decay rates could most simply arise from an increase in the distance between the H• donor and acceptor. Positioning the substrate away from the ferryl oxygen would also likely diminish the efficiency of HO• rebound and could thereby enable the competing Cl• transfer in the subsequent step. These

observations led to the hypothesis that substrate positioning controls outcome in SyrB2, with the native **Thr** being held farther away from the ferryl oxygen and closer to the halogen to trade proficiency in H• abstraction for selectivity in ligand-radical transfer.³⁶ This hypothesis was supported by the nearly complete reversal of the outcome for **Nva** from hydroxylation of C5 to chlorination of C4 by deuterium (D) substitution at C5. With neither or both positions deuterium-labeled, the chloroferryl complex abstracts H(D) more rapidly from C5, but, with only C5 labeled, the C4 position is targeted more rapidly, due to the large kinetic isotope effect disfavoring D• abstraction. Redirection to C4 results in more chlorination than hydroxylation (~ 4:1), as rationalized by the positioning hypothesis.³⁶

To date, no experimental structural data to evaluate the substrate-positioning hypothesis have been reported. The nature and magnitude of repositioning that might be required to explain the observed effects on reactivity are thus unknown. Moreover, recent theoretical work has suggested that interchange of the oxygen and chloride ligands relative to their positions in the crystal structure could also contribute to the control of outcome.^{37,38} According to these studies, the substrate dictates both the chloro/oxo disposition and the frontier orbitals involved in the H•-abstraction step, with the engagement of π - or σ -type ferryl orbitals favoring Cl• or HO• transfer, respectively.³⁸ Although not incompatible with the positioning hypothesis, this idea would imply that the differential reactivity observed for the different substrates might arise primarily from substrate-protein interactions that impact the partition between the axial and equatorial coordination isomers of the ferryl complex rather than from substrate positioning *per se*.

Given the possibility that these other factors might be involved in directing the halogenation outcome and the likelihood that proper substrate positioning is also essential to avoidance of hydroxylation in the other types of Fe/2OG-oxygenase reactivity, we sought to directly probe the positions of the various target C-H bonds relative to the iron center. Electron paramagnetic resonance (EPR) spectroscopy can resolve relatively weak interactions between unpaired electrons (e.g., centered on a metallocofactor) and nearby magnetic nuclei (e.g. ^1H , ^{14}N). Unfortunately, all of the species in the catalytic cycle of SyrB2 that have been characterized to date have integer spin states [several high-spin ($S = 2$) Fe(II) forms and the high-spin ($S = 2$) haloferryl complex], and therefore cannot be addressed by conventional, perpendicular-mode EPR methods. Therefore, in order to obtain an EPR-active probe in the active site, an Fe-NO complex was generated (Figure 2A).^{39–41} Nitric oxide (NO•) has been employed as an analog of O₂ that binds to Fe(II) complexes to form an $S = 3/2$ iron-nitrosyl complex (denoted {Fe-NO}⁷)⁴² best described as a high-spin Fe(III) center ($S = 5/2$) antiferromagnetically coupled to NO[−] ($S = 1$).^{43–45} This complex is thought to be analogous to the putative {Fe-OO}⁸ intermediate in the catalytic cycle,^{43,46} and previous studies on taurine:2OG dioxygenase (TauD) have employed such complexes in combination with pulse EPR methods to determine the position of substrate C-H bonds.^{40,41} In this work, we employed hyperfine sublevel correlation (HYSCORE) spectroscopy to obtain geometric information about the active site of SyrB2 by measuring hyperfine couplings to specifically ^2H -labeled **Thr**, **Aba**, and **Nva** substrates. The magnitude and orientation dependence of these hyperfine parameters provide spatial information about the labeled position relative to the metallocofactor; these data represent the first experimental

structural data on the SyrB2:aminoacyl-SyrB1 complex and reveal the nature and extent of repositioning in the SyrB2 substrates exhibiting such widely divergent reactivities.

Results

When the complex of SyrB2 with its substrates is exposed to gaseous NO, a dark yellow complex characterized by an almost axial EPR signal (Figure 2B) with principal g_{eff} values of 4.06, 3.99, and 2.00 is produced. These parameters are typical of $\{\text{Fe-NO}\}^7$ complexes with $S = 3/2$ ground states and minor rhombicity in the zero-field splitting.^{40,41,43} Figure 3A shows a Q-band HYSCORE spectrum collected for the $\{\text{Fe-NO}\}^7$ form of SyrB2 in complex with SyrB1 presenting 4,4,5,5,5- $[\text{}^2\text{H}_5]$ -L-norvaline (hereafter abbreviated **NO-4,5- d_5 -Nva**). In ^2H -HYSCORE spectra, hyperfine coupling is manifest as splitting along the anti-diagonal, centered on the deuterium Larmor frequency; in addition, further splitting along the diagonal is observed due to the nuclear quadrupole interaction (Figure 2D). At $g_{eff} = 3.98$ (~613 mT), the observed HYSCORE spectrum exhibits such a signal, centered at the deuterium Larmor frequency (4.0 MHz; Figure 3A). Comparison with the same spectrum collected for a sample prepared with all-protium norvaline (**NO-Nva**) reveals that this feature is attributable to deuterium (Figure 3D). Additional features are observed in all measured spectra (Figure S1), and are attributed to matrix protons and ^{14}N nuclei (e.g. from the histidine ligands and/or from NO), consistent with previous observations on similar systems.⁴⁰ For the **NO-4,5- d_5 -Nva** complex, it is ambiguous whether the ^2H -HYSCORE signals arise from interactions with deuterium nuclei at C4, C5, or both positions. However, the spectrum of the complex prepared with 5,5,5- $[\text{}^2\text{H}_3]$ -Nva (**NO-5- d_3 -Nva**) at $g_{eff} = 3.98$ (Figure 3B) reveals features that are essentially identical to those of **NO-4,5- d_5 -Nva**. Moreover, spectra of the **NO-4- d_2 -Nva** complex have features with visibly reduced width and intensity compared to either **NO-4,5- d_5 -Nva** or **NO-5- d_3 -Nva** (Figure 3C). Therefore, the signals observed for **NO-4,5- d_5 -Nva** are attributed to deuterons at the C5 position.

Because the deuterium nuclei of interest lie along a particular vector in the active site, the hyperfine interaction will have an angular dependence with respect to the electronic \mathbf{g} -tensor (Figure 2C and 2D). In order to ascertain this angular dependence, HYSCORE spectra for **NO-4,5- d_5 -Nva** were collected at multiple magnetic fields (Figure S2), corresponding to excitation of different orientational sub-populations of spins (Figure 2C). For all spectra collected, signals for **NO-4,5- d_5 -Nva** and **NO-5- d_3 -Nva** were essentially identical (Figure S3), and were simulated by a single axial hyperfine coupling with magnitude $T = 0.40 \pm 0.05$ MHz and quadrupole coupling constant $K = 0.035 \pm 0.005$ MHz (Table S1, Figures S2 and S3). The ability of a single deuterium hyperfine coupling (rather than three) to adequately account for the observed spectra likely reflects rotational averaging of the three C5 deuterons. In similar fashion, field-dependent spectra of **NO-4- d_2 -Nva** were simulated with parameters $T = 0.28 \pm 0.05$ MHz and $K = 0.025 \pm 0.005$ MHz (Table S1, Figure S4).

Field-dependent HYSCORE spectra of the NO complex formed with the substrate **2,3,3,4,4,4- $[\text{}^2\text{H}_6]$ -Aba** (**NO- per - d_6 -Aba**) reveal deuterium features that are visibly less broad than those arising from **NO-4,5- d_5 -Nva**, suggesting that, in this sample, the hyperfine interactions are weaker and the deuterium nuclei more distant from the $\{\text{Fe-NO}\}^7$ moiety (Figures 4A and S5). As in the case of **Nva**, the spectral features of the **NO- per - d_6 -Aba**

complex arise primarily from the methyl deuterons. This fact, established by the weaker and narrower signals from the **NO-3-*d*₂-Aba** complex (Figure 4B), shows that the deuterium nuclei at C4 are the closest to the {Fe-NO}⁷ unit, consistent with the known ability of C4 but not C3 to donate H• to the ferryl intermediate.³⁵ Although, in principle, the spectrum of **NO-*per-d*₆-Aba** may also contain some contribution from the single deuteron at C2, the complete inactivity of C2 for H• donation to the ferryl in multiple different non-native substrates suggests that this contribution should be negligible. The spectra for **NO-*per-d*₆-Aba** were simulated with axial hyperfine and quadrupole coupling tensors with magnitude $T = 0.29 \pm 0.04$ MHz and $K = 0.050 \pm 0.005$ MHz, respectively (Table S1, Figure S5). Spectra collected for **NO-3-*d*₂-Aba** were simulated with $T = 0.14 \pm 0.02$ MHz and $K = 0.043 \pm 0.005$ MHz (Table S1, Figure S6).

The native substrate of SyrB2, **Thr**, is almost exclusively chlorinated, and determination of the position of this substrate relative to the cofactor is of particular interest. Therefore, field-dependent HYSCORE spectra of the NO complex formed with the substrate **2,3,4,4,4-[²H₅]-Thr (NO-*per-d*₅-Thr)** were recorded. These spectra are similar to the spectra of **NO-*per-d*₆-Aba**, although the ²H signals are discernibly less broad (Figure 5A). Spectra were also collected for the complex prepared with **2,3-*d*₂-Thr** (Figure 5B). As in the case of **Aba** and **Nva**, the absence of deuteria on the terminal methyl group results in diminished width and intensity of the ²H HYSCORE crosspeaks (Figure 5), thus allowing assignment of the majority of the ²H signals in the **NO-*per-d*₅-Thr** spectrum to deuterons on C4. The field-dependent spectra of **NO-*per-d*₅-Thr** were simulated with $T = 0.20 \pm 0.03$ MHz and $K = 0.040 \pm 0.005$ MHz (Table S1, Figure S7). Signals for **NO-2,3-*d*₂-Thr**, which we attribute primarily to the single deuteron at the C3 position, were simulated with $T = 0.15 \pm 0.03$ MHz and $K = 0.043 \pm 0.005$ MHz (Figure S8).

In previous studies on {Fe-NO}⁷ complexes in enzymes, the point-dipole approximation has been used to relate the magnitude of the hyperfine coupling to an Fe-²H distance, with the second hyperfine Euler angle (θ) roughly corresponding to the (O)N-Fe-²H angle.³⁹⁻⁴¹ To provide more accurate Fe-²H distance and N-Fe-²H angle estimates, we instead developed a geometric model that accounts for spin-density distribution across the Fe-NO unit, with explicit dipolar contributions from both the ferric and NO⁻ species (see Materials and Methods). Analyzed by this model, the observed hyperfine parameters correspond to Fe-²H distances of 4.2 ± 0.3 Å, 3.7 ± 0.2 Å, 3.7 ± 0.3 Å and 3.4 ± 0.3 Å, and N-Fe-²H angles of 85 ± 10 , 85 ± 10 , 81 ± 15 , and 64 ± 7 degrees for **NO-*per-d*₅-Thr**, **NO-*per-d*₆-Aba**, **NO-4-*d*₂-Nva**, and **NO-4,5-*d*₅-Nva**, respectively (Table S2, Figure 6B).

Discussion

Comparison of the hyperfine coupling constants for the methyl groups of the three substrates investigated reveals a striking trend (Figure 6A). The magnitude of the hyperfine coupling increases significantly through the series: **NO-*per-d*₅-Thr** (0.20 MHz), **NO-*per-d*₆-Aba** (0.29 MHz), **NO-4,5-*d*₅-Nva** (0.40 MHz), corresponding to distances of 4.2 Å, 3.7 Å, and 3.4 Å, respectively. The observed deuterium positions are fully consistent with the trends in H•-abstraction rate constants and chlorination selectivity previously reported for these substrates. **Nva** is the most efficient H• donor to the ferryl complex and is closest to the

metallocofactor (3.4 Å). H• transfer from **Thr**, 0.8 Å farther away, is markedly (130-fold) slower. The observed distances for **NO-4-d₂-Nva** and **NO-per-d₆-Aba** are very similar, just as the reactivities of C4 of **Aba** and **Nva** are similar. Finally, the hyperfine couplings observed for **NO-3-d₂-Aba** and **NO-2,3-d₂-Thr** correspond to distances of 4.7 ± 0.3 Å and 4.7 ± 0.4 Å, respectively, consistent with published observations that the chloroferryl complex in SyrB2 does not target the C3 position (e.g., of **Ala**).³⁵

The N-Fe-D angle of 85° implies that the target deuterons of **Thr** lie nearly in the plane perpendicular to the Fe-N bond (Figure 6B). Under the simplest assumption, the oxo group of the ferryl complex and hydroxo ligand of the Fe(III)-OH/substrate-radical state would reside in approximately the same location as the nitrosyl ligand (Figure 1). This disposition of substrate and cofactor would also help to rationalize the reactivity data. As shown by computational studies, the nearly orthogonal Fe=O/C-H orientation would result in poor orbital overlap and would thus be expected to afford relatively inefficient H• abstraction, as observed for **Thr**. The large angle would then also place the substrate radical relatively far from the hydroxo ligand and potentially much closer to the chloro ligand, which is also expected to lie in the plane perpendicular to the Fe-N bond (Figure 6B). The predominant chlorination observed for **Thr** would thus be rationalized. It should be noted that the position of the Cl⁻ ligand *within* the plane perpendicular to the Fe-N bond cannot be determined from these data; however, based on the observation of Cl• transfer, it is likely that the target ²H is close to the Cl⁻ (i.e. that the Cl-Fe-N-²H dihedral angle is small). Intriguingly, the relatively modest structural perturbations observed for **Nva**, including a ~0.8 Å closer approach and ~20° tilt towards the Fe-N(O) bond, are sufficient to largely unleash both the H•-abstraction potency of the ferryl and the default hydroxylation outcome. Although **NO-per-d₅-Thr**, **NO-per-d₆-Aba**, and **NO-4-d₂-Nva** all exhibit similar angles (80–85°), the C4 carbons of both **Nva** and **Aba** nevertheless exhibit a partial loss of selectivity, undergoing a mixture of hydroxylation and chlorination. As previously suggested, this difference is potentially attributable to the shorter average distance of the C4 carbon in the non-native substrates from the cofactor (shown here to be the ~0.5 Å), to greater flexibility of the non-native side-chains for dynamic approach, or to both. As the only structural distinction between **Thr** and **Aba**, the β-hydroxyl group of **Thr** seemingly must serve to anchor the native side chain (e.g., *via* hydrogen bonding) either to enforce the greater distance or to restrict its dynamics (or both). Elucidation of this interaction could provide avenues for rational design to promote halogenation of alternative substrates.

Overall, the striking correlation between the observed distances and angles and the reactivity patterns of **Thr**, **Aba**, and **Nva** strongly corroborates the assertion that substrate positioning controls chemoselectivity in SyrB2. These data do not rule out the possibility that coordination isomerism also contributes to selectivity, but the magnitude of the differences in positioning observed in this study strongly suggests that substrate positioning exerts a major influence. In addition, our measurements define this differential positioning; the native substrate is held close to the chloride in the plane perpendicular to the Fe-N(O) bond, but at a greater distance from the iron center compared to the non-native substrates. The result of this careful positioning of the native substrate is relatively sluggish H• abstraction by the ferryl intermediate but high chlorination selectivity in the ligand-transfer step.

Although these experiments define the position of the substrate, the interactions which dictate this positioning remain unknown. The large angle observed for **NO-per-d₅-Thr** is not obviously consistent with previous docking models together with the simplest assumption that NO would replace the water ligand in the published x-ray crystal structure³² (Figure S9A).³⁷ However, NO coordination at one of the two sites occupied in the crystal structure by the chloride ion and by C1 of 2OG could result in the observed angle (Figure S9B and S9C). The latter of these two NO binding modes has been observed in clavaminase synthase.⁴⁷ Our results thus imply that, for the docking model to be correct, a shift of the Cl⁻ ligand or the 2OG carboxylate must accompany addition of NO, and, by analogy, possibly also O₂, to the Fe(II) cofactor. Alternatively, it is also possible that SyrB1 may bind in a different manner that places the substrate at the observed angle when NO adds at the position of the water. This question emphasizes the importance of further structural characterization of the SyrB1:SyrB2 complex.

Finally, the measurement of substrate placement for carbon centers undergoing different outcomes maps the transition from hydroxylation to halogenation; these parameters potentially provide a geometric map for the promotion or suppression of hydroxylation in the Fe/2OG reaction manifold. The striking conclusion is that relatively stringent control of substrate position is required to suppress the hydroxylation outcome. We suggest that these parameters establish guiding metrics for analyzing other alternative reactions catalyzed by members of the Fe/2OG family. By comparison of substrate positions in other enzymes with the parameters reported here, cases (e.g., olefin-installing 1,2-dehydrogenations in biosyntheses of antibiotics) in which hydroxylation might or might not be part of the mechanistic pathway can now be analyzed to ascertain whether these poorly understood alternative outcomes arise from avoiding HO• rebound (as in the SyrB2 reaction) or from further processing of a hydroxylated intermediate in a “cryptic hydroxylation” mechanism.

Conclusion

Hyperfine couplings have been measured between a series of deuterium labeled substrates and an active-site {Fe-NO}⁷ complex of the Fe/2OG aliphatic halogenase, SyrB2. Analysis of these parameters provides the first experimental structural data on the complex of an Fe/2OG halogenase with its substrate. The methyl groups of the substrates **Thr**, **Aba**, and **Nva** lie 4.2 Å, 3.7 Å, and 3.4 Å from the metallocofactor (Fe-D distance), explaining the previously observed trend in rates of H• abstraction and chlorination-versus-hydroxylation selectivity. In addition, the distances observed for adjacent positions (C3 of **Thr** and **Aba** and C4 of **Nva**) are also consistent with expectations from reactivity studies. The results, along with the analogy of the iron-nitrosyl complex to oxygen-bound intermediates in the catalytic cycle, substantiate the hypothesis that substrate positioning controls reaction outcome in SyrB2 catalysis. Both a relatively long Fe-D distance and almost perpendicular N-Fe-D angle conspire to promote chlorination of the native substrate, **Thr**. Moreover, the structural parameters for targets spanning the continuum of SyrB2 reactivity, from almost pure halogenation to predominant hydroxylation, lay a foundation for the investigation of how other Fe/2OG enzymes are able to direct other reactions in the diverse array catalyzed by this important enzyme family.

Materials and Methods

Materials

Commercially available materials were used without further purification. 2,3,4,4,4- $^{2}\text{H}_5$ -L-threonine was purchased from Cambridge Isotope Laboratories. 4,4,5,5,5- $^{2}\text{H}_5$ -L-norvaline, 2,3,3,4,4,4- $^{2}\text{H}_6$ -L-2-aminobutyric acid, 3,3- $^{2}\text{H}_2$ -L-2-aminobutyric acid, and 2,3- $^{2}\text{H}_2$ -L-threonine were purchased from C/D/N isotopes. 5,5,5- $^{2}\text{H}_3$ -L-norvaline and 4,4- $^{2}\text{H}_2$ -L-norvaline were synthesized as described elsewhere.³⁶

Generation of the Substrate-Bound {Fe-NO}⁷ Complexes

SyrB2 and SyrB1 were prepared, and SyrB1 was charged with the desired amino acid, as previously described.³⁵ Aminoacyl-S-SyrB1 and SyrB2 were deoxygenated separately as previously described. After deoxygenation, SyrB2, Fe(II), Cl^- , 2OG, and aminoacyl-S-SyrB1 were mixed in a MBraun (Stratham, NH) anoxic chamber to final concentrations of 1.25 mM, 1.15 mM, 10 mM, 5 mM, and 1.6 mM, respectively. The resulting solution was returned to the Schlenk line; the flask was briefly evacuated to ~100 Torr and slowly refilled with nitric oxide gas (Messer) to > 900 Torr. Under this atmosphere, the protein was incubated on ice with brisk stirring for 10 min, as the dark yellow color developed. The resulting complex was concentrated anaerobically by spin filtration to approximately half its original volume (~15 min), transferred to an EPR tube, and frozen in liquid nitrogen.

Electron Paramagnetic Resonance Measurements

Continuous wave (CW) and pulse EPR spectra were acquired on a Bruker Elexsys E580 spectrometer equipped with a SuperX-FT microwave bridge. CW spectra were acquired at X-band frequencies using a Bruker SHQE resonator. A temperature of 7 K was maintained with an ER 4112-HV Oxford Instruments liquid helium flow cryostat.

Field-swept pulse EPR and HYSCORE spectra were acquired at Q-band frequencies by using a home-built intermediate-frequency extension of the SuperX-FT X-band bridge that has a Millitech 5W pulse power amplifier. All experiments were conducted on a home-built TE₀₁₁ resonator utilizing the open resonator concept developed by Annino et al.⁴⁸ and mechanical construction of the probehead similar to that presented by Reijerse et al.⁴⁹ This setup allows $t(\pi/2) = 12\text{--}16$ ns at maximum input power with spectrometer dead time (including the resonator ring time) of 100–120 ns. Data acquisition and control of experimental parameters were performed by using Bruker XEPR software.

HYSCORE Spectra

HYSCORE spectra were obtained using the standard HYSCORE program available in the XEPR software, with the exception of HYSCORE spectra collected at 950 mT. For standard HYSCORE measurements, the parameters $t(\pi/2) = 8$ ns and $\tau = 140$ ns (variables defined in Figure S10) were used. HYSCORE spectra at 950 mT were collected using the matched HYSCORE technique utilizing a PulseSpel program in XEPR.⁵⁰ In the latter case, the length of the second and fourth $\pi/2$ pulses was adjusted to match the ^2H Larmor frequency of 6.2 MHz, $t_m \approx 40$ ns (Figure S10). For this purpose the pulses were generated by the secondary pulse forming unit (i.e., using the $\pm<x>$ channels) and attenuated to allow for $t(\pi/2) = 40$ ns.

Unless otherwise noted, spectra were collected with a 28 ns step size and with 300 points (602, 613, and 700 mT) or 200 points (950 mT) in the x and y dimensions. Shot repetition time was set to 50 μ s, with 100 shots per point. Typical number of scans averaged was: 6 (602 mT), 3 (613 mT), 12 (700 mT), and 45 (950 mT). A standard four-step phase cycle was used in all cases. Additional experimental parameters are reported in the figure legends.

Data Analysis

Data processing and spectral simulations were performed using Kazan viewer, a homewritten suite of utilities in MATLAB.⁵¹ One-dimensional EPR simulations were performed using the “pepper” utility from the EasySpin software package.⁵² HYSCORE data were analyzed by simultaneous frequency domain simulation of all field-dependent spectra until a satisfactory solution was achieved. To reduce the number of fitting variables, a purely axial point-dipolar model of the ^2H hyperfine interaction was used:

$$\mathbf{A} = [-1, -1, 2] \mathbf{T} \quad (1)$$

where \mathbf{T} is the magnitude of the interaction. In addition, the quadrupole coupling was assumed to be purely axial; thus, the following principal values of the quadrupole coupling were used:

$$\mathbf{Q} = [-1, -1, 2] \mathbf{K} \quad (2)$$

where $\mathbf{K} = \text{eqQ}/[4I(2I+1)h]$, eqQ is the strength of the electric field gradient, and I is the nuclear spin quantum number ($I = 1$ for ^2H). In the case of **NO-*per-d*₆-Aba** and **NO-4-*d*₂-Nva**, the axial quadrupole interaction was found to be insufficient, and an additional fitting variable η was introduced such that

$$\mathbf{Q}_{x,y,z} = [-1-\eta, -1+\eta, 2] \mathbf{K} \quad (3)$$

Details of the parameters used to simulate the experimental data are provided in Table S1. The orientation of a given tensor is defined by the Euler angles (y convention) φ , θ , and ψ . In axial tensors, the φ angle is meaningless and was not included in any simulations. Uncertainty analysis was performed by stepwise alteration of a given parameter until the fit quality was unacceptable by visual inspection. Both fits and uncertainty analysis were confirmed by construction of one-dimensional “skyline” plots. These plots were constructed with the skyline along the anti-diagonal of the HYSCORE plot, in order to remove width contributions arising from quadrupolar interactions (Figure S11).

Distance and angle information was obtained by constructing a model which accounts for hyperfine coupling of the deuterium nucleus with the $S = 1$ NO^- species and the $S = 5/2$ ferric species. Distances and angles fixed on the basis of studies on model complexes were: Fe-N = 1.75 Å, N-O = 1.14 Å.⁵³ Varying the Fe-N-O angle from 120–180° and the O-N-Fe- ^2H dihedral from 0–180° produced small deviations relative to the uncertainty in simulation of the hyperfine parameters. The reported parameters are for Fe-N-O = 150° and O-N-Fe- ^2H = 180° (Figure S12). The z-component of the ground state \mathbf{g} -tensor was assumed to lie along the Fe-N bond.⁴³ For a given deuterium position, dipolar coupling tensors \mathbf{A}_{FeD} ,

A_{OD} , and A_{ND} were computed, using eq. (1) to calculate the principal components of the tensors with magnitude, T_{XD} , according to the formula:

$$T_{XD}(\text{MHz}) = 12.1362 r_{XD}^{-3} \quad (4)$$

Then, the individual tensors were oriented along the corresponding X-D vectors and combined, accounting for the appropriate spin-projection factors and assuming equal spin density on nitrogen and oxygen:

$$\mathbf{A}_{\text{tot}} = 7/5 \mathbf{A}_{\text{FeD}} - 2/5 (0.5 \mathbf{A}_{\text{OD}} + 0.5 \mathbf{A}_{\text{ND}}) \quad (5)$$

where 7/5 and -2/5 are the spin-projection factors for iron and NO, respectively.⁵⁴ In addition, the \mathbf{A}_{tot} tensor was rotated according to the third Euler angle (ψ) in the orientation of the experimentally derived hyperfine tensors. The Fe-²H distance and N-Fe-²H angle were then varied to match the experimentally observed hyperfine tensor (see Tables S1 & S2).

Supplementary Material

Refer to Web version on PubMed Central for supplementary material.

Acknowledgments

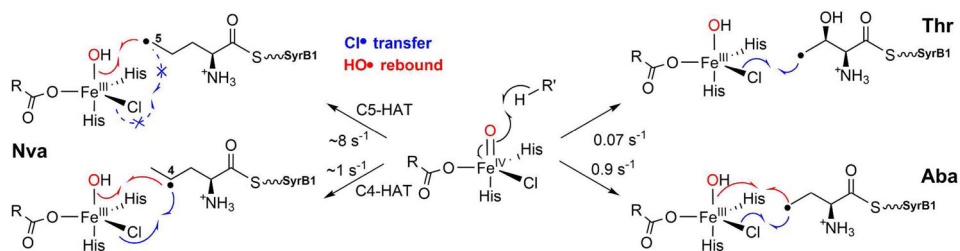
R. J. M. gratefully acknowledges the support of the Schriesheim Distinguished Graduate Fellowship (Pennsylvania State University). This work was supported by the National Institutes of Health (GM-69657 to C.K. and J.M.B.) and the National Science Foundation (MCB-642058 and CHE-724084 to C.K. and J.M.B.).

Literature Cited

- Solomon EI, Brunold TC, Davis MI, Kemsley JN, Lee SK, Lehnert N, Neese F, Skulan AJ, Yang YS, Zhou J. Chem Rev. 2000; 100:235–350. [PubMed: 11749238]
- Hausinger RP. Crit Rev Biochem Mol Biol. 2004; 39:21–68. [PubMed: 15121720]
- Costas M, Mehn MP, Jensen MP, Que L Jr. Chem Rev. 2004; 104:939–986. [PubMed: 14871146]
- Krebs C, Galoni Fujimori D, Walsh CT, Bollinger JM Jr. Acc Chem Res. 2007; 40:484–492. [PubMed: 17542550]
- Wallar BJ, Lipscomb JD. Chem Rev. 1996; 96:2625–2658. [PubMed: 11848839]
- Krebs C, Bollinger JM Jr, Booker SJ. Curr Opin Chem Biol. 2011; 15:291–303. [PubMed: 21440485]
- Green MT. Curr Opin Chem Biol. 2009; 13:84–88. [PubMed: 19345605]
- Frey PA, Hegeman AD, Ruzicka FJ. Crit Rev Biochem Mol Biol. 2008; 43:63–88. [PubMed: 18307109]
- Booker SJ. Curr Opin Chem Biol. 2009; 13:58–73. [PubMed: 19297239]
- Ivan M, Kondo K, Yang H, Kim W, Valiando J, Ohh M, Salic A, Asara JM, Lane WS Jr, WGK. Science. 2001; 292:464–468. [PubMed: 11292862]
- Jaakkola P, Mole DR, Tian Y-M, Wilson MI, Gielbert J, Gaskell SJ, von Kriegsheim A, Hebestreit HF, Mukherji M, Schofield CJ, Maxwell PH, Pugh CW, Ratcliffe PJ. Science. 2001; 292:468–472. [PubMed: 11292861]
- Gerken T, Girard CA, Tung YCL, Webby CJ, Saudek V, Hewitson KS, Yeo GSH, McDonough MA, Cunliffe S, McNeill LA, Galvanovskis J, Rorsman P, Robins P, Prieur X, Coll AP, Ma M,

- Jovanovic Z, Farooqi IS, Sedgwick B, Barroso I, Lindahl T, Ponting CP, Ashcroft FM, O'Rahilly S, Schofield CJ. *Science*. 2007; 318:1469–1472. [PubMed: 17991826]
13. Treweek SC, Henshaw TF, Hausinger RP, Lindahl T, Sedgwick B. *Nature*. 2002; 419:174–178. [PubMed: 12226667]
14. Falnes PØ, Johansen RF, Seeberg E. *Nature*. 2002; 419:178–182. [PubMed: 12226668]
15. Yi C, Jia G, Hou G, Dai Q, Zhang W, Zheng G, Jian X, Yang CG, Cui Q, He C. *Nature*. 2010; 468:330–333. [PubMed: 21068844]
16. Tsukada Y, Fang J, Erdjument-Bromage H, Warren ME, Borchers CH, Tempst P, Zhang Y. *Nature*. 2006; 439:811–816. [PubMed: 16362057]
17. Klose RJ, Yamane K, Bae Y, Zhang D, Erdjument-Bromage H, Tempst P, Wong J, Zhang Y. *Nature*. 2006; 442:312–316. [PubMed: 16732292]
18. Cloos PAC, Christensen J, Agger K, Maiolica A, Rappsilber J, Antal T, Hansen KH, Helin K. *Nature*. 2006; 442:307–311. [PubMed: 16732293]
19. Que L Jr. *Nat Struct Mol Biol*. 2000; 7:182–184.
20. Koehntop KD, Emerson JP, Que L Jr. *J Biol Inorg Chem*. 2005; 10:87–93. [PubMed: 15739104]
21. Price JC, Barr EW, Tirupati B, Bollinger JM Jr, Krebs C. *Biochemistry*. 2003; 42:7497–7508. [PubMed: 12809506]
22. Hoffart LM, Barr EW, Guyer RB, Bollinger JM Jr, Krebs C. *Proc Natl Acad Sci U S A*. 2006; 103:14738–14743. [PubMed: 17003127]
23. Proshlyakov DA, Henshaw TF, Monterosso GR, Ryle MJ, Hausinger RP. *J Am Chem Soc*. 2004; 126:1022–1023. [PubMed: 14746461]
24. Riggs-Gelasco PJ, Price JC, Guyer RB, Brehm JH, Barr EW, Bollinger JM Jr, Krebs C. *J Am Chem Soc*. 2004; 126:8108–8109. [PubMed: 15225039]
25. Price JC, Barr EW, Glass TE, Krebs C, Bollinger JM Jr. *J Am Chem Soc*. 2003; 125:13008–13009. [PubMed: 14570457]
26. Hanauske-Abel HM, Günzler V. *J Theor Biol*. 1982; 94:421–455. [PubMed: 6281585]
27. Groves JT. *J Chem Educ*. 1985; 62:928–931.
28. Vaillancourt FH, Yin J, Walsh CT. *Proc Natl Acad Sci U S A*. 2005; 102:10111–10116. [PubMed: 16002467]
29. Vaillancourt FH, Vosburg DA, Walsh CT. *Chem Bio Chem*. 2006; 7:748–752.
30. Galoni DP, Vaillancourt FH, Walsh CT. *J Am Chem Soc*. 2006; 128:3900–3901. [PubMed: 16551084]
31. Vaillancourt FH, Yeh E, Vosburg DA, O'Connor SE, Walsh CT. *Nature*. 2005; 436:1191–1194. [PubMed: 16121186]
32. Blasiak LC, Vaillancourt FH, Walsh CT, Drennan CL. *Nature*. 2006; 440:368–371. [PubMed: 16541079]
33. Galoni DP, Barr EW, Walsh CT, Bollinger JM Jr, Krebs C. *Nat Chem Biol*. 2007; 3:113–116. [PubMed: 17220900]
34. Galoni Fujimori D, Barr EW, Matthews ML, Koch GM, Yonce JR, Walsh CT, Bollinger JM Jr, Krebs C, Riggs-Gelasco PJ. *J Am Chem Soc*. 2007; 129:13408–13409. [PubMed: 17939667]
35. Matthews ML, Krest CM, Barr EW, Vaillancourt FH, Walsh CT, Green MT, Krebs C, Bollinger JM Jr. *Biochemistry*. 2009; 48:4331–4343. [PubMed: 19245217]
36. Matthews ML, Neumann CS, Miles LA, Grove TL, Booker SJ, Krebs C, Walsh CT, Bollinger JM Jr. *Proc Natl Acad Sci U S A*. 2009; 106:17723–17728. [PubMed: 19815524]
37. Borowski T, Noack H, Rado M, Zych K, Siegbahn PEM. *J Am Chem Soc*. 2010; 132:12887–12898. [PubMed: 20738087]
38. Wong SD, Srncic M, Matthews ML, Liu LV, Kwak Y, Park K, Bell CBI, Alp EE, Zhao J, Yoda Y, Kitao S, Seto M, Krebs C, Bollinger JM Jr, Solomon EI. *Nature*. 2013; 499:320–323. [PubMed: 23868262]
39. Yang TC, Wolfe MD, Neibergall MB, Mekmouche Y, Lipscomb JD, Hoffman BM. *J Am Chem Soc*. 2003; 125:7056–7066. [PubMed: 12783560]

40. Muthukumaran RB, Grzyska PK, Hausinger RP, McCracken J. *Biochemistry*. 2007; 46:5951–5959. [PubMed: 17469855]
41. Casey TM, Grzyska PK, Hausinger RP, McCracken J. *J Phys Chem B*. 2013; 117:10384–10394. [PubMed: 23937570]
42. Enemark JH, Feltham RD. *Coord Chem Rev*. 1974; 13:339–406.
43. Brown CA, Pavlosky MA, Westre TE, Zhang Y, Hedman B, Hodgson KO, Solomon EI. *J Am Chem Soc*. 1995; 117:715–732.
44. Hauser C, Glaser T, Bill E, Weyhermüller T, Wieghardt K. *J Am Chem Soc*. 2000; 122:4352–4365.
45. Ye S, Price JC, Barr EW, Green MT, Bollinger JM Jr, Krebs C, Neese F. *J Am Chem Soc*. 2010; 132:4739–4751. [PubMed: 20218714]
46. Ye S, Riplinger C, Hansen A, Krebs C, Bollinger JM Jr, Neese F. *Chem-Eur J*. 2012; 18:6555–6567. [PubMed: 22511515]
47. Zhang Z, Ren J, Harlos K, McKinnon CH, Clifton IJ, Schofield CJ. *FEBS Lett*. 2002; 517:7–12. [PubMed: 12062399]
48. Annino G, Cassettari M, Martinelli M. *IEEE Trans Microw Theory Tech*. 2009; 57:775–783.
49. Reijerse E, Lendzian F, Isaacson R, Lubitz W. *J Magn Reson*. 2012; 214:237–243. [PubMed: 22196894]
50. Jeschke G, Rakhmatullin R, Schweiger A. *J Magn Reson*. 1998; 131:261–271. [PubMed: 9571102]
51. [accessed May 7, 2015] Kazan Viewer - Homepage Alexey Silakov. <https://sites.google.com/site/silakovalexey/kazan-viewer>
52. Stoll S, Schweiger A. *J Magn Reson*. 2006; 178:42–55. [PubMed: 16188474]
53. Westre TE, Di Cicco A, Filipponi A, Natoli CR, Hedman B, Solomon EI, Hodgson KO. *J Am Chem Soc*. 1994; 116:6757–6768.
54. Bencini, A.; Gatteschi, D. *EPR of Exchange Coupled Systems*. Springer-Verlag; Berlin: 1990.

**Figure 1.**

Divergent reactivity of the SyrB2 ferryl intermediate upon SyrB1 presenting different amino acids: threonine (**Thr**), top right; aminobutyric acid (**Aba**), bottom right; norvaline (**Nva**), left. Red arrows depict hydroxylation, whereas blue arrows depict halogenation. R = CH₂CH₂COOH.

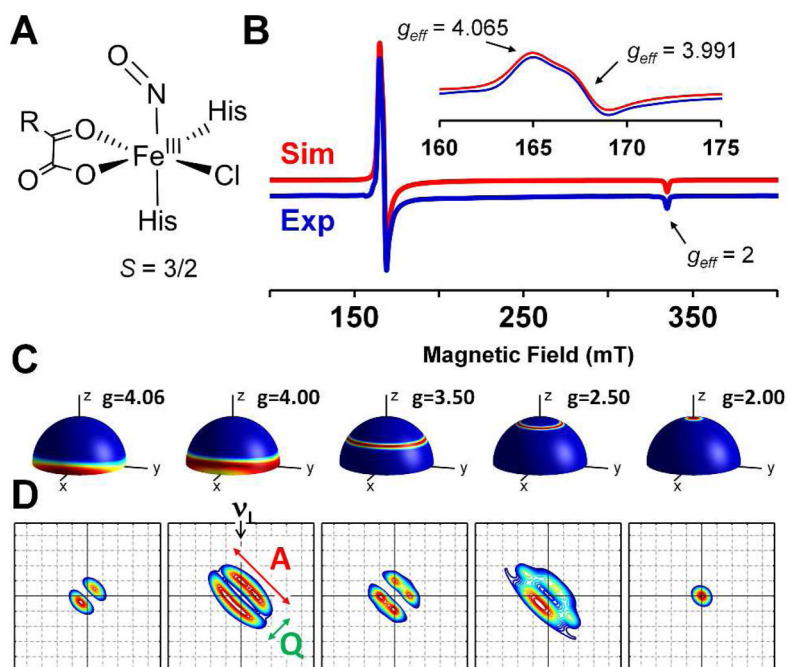


Figure 2. Chemical structural representation (A) and continuous-wave, X-band EPR spectrum (B) of the {Fe-NO}⁷ form of SyrB2 in complex with aminoacyl-SyrB1. R = CH₂CH₂COOH. Experimental spectrum (blue) and simulation (red, shifted upwards for clarity). Inset, expanded view of the $g_{eff} = 4$ region of the spectrum. C) orientation selectivity pattern calculated for various magnetic fields using “RGB” color coding (red - fully excited, blue - not excited). Corresponding effective g -values are shown to the right of each hemisphere. D) HYSCORE spectra calculated using orientation selectivity patterns from panel C and spin Hamiltonian parameters for NO-4,5-*d*₅-Nva from Table S1. Splitting due to hyperfine coupling (A) and quadrupole coupling (Q) is indicated in the $g = 4$ spectrum.

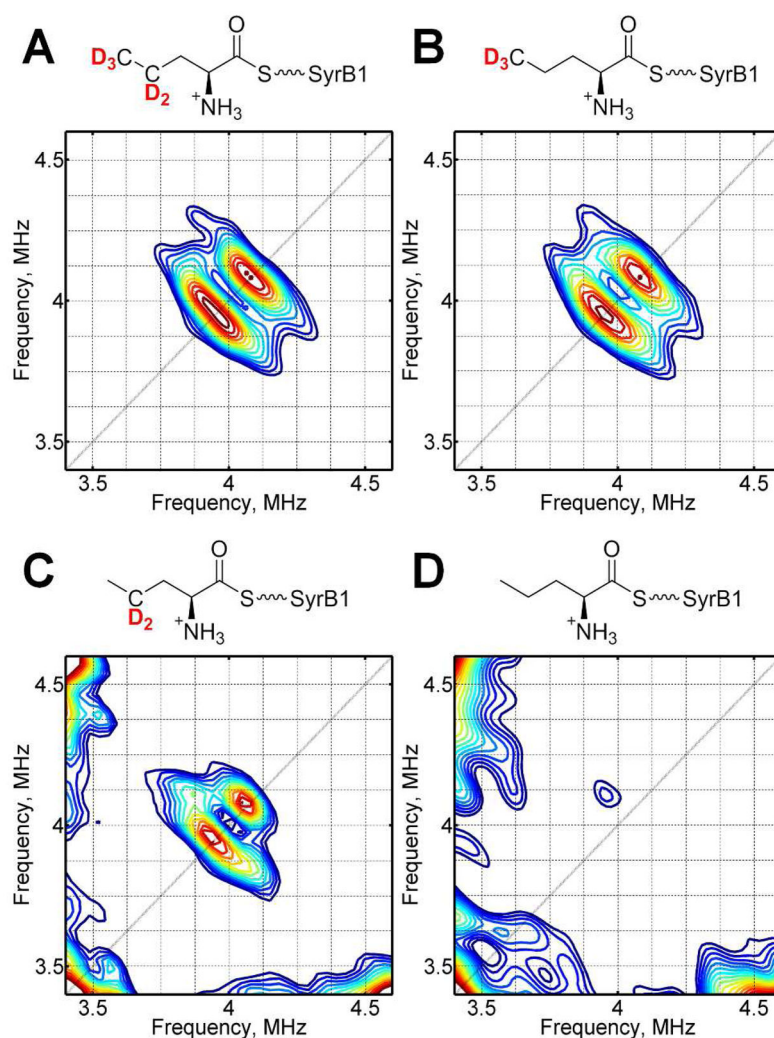


Figure 3. HYSORE spectra and substrate chemical structures for A) **NO-4,5- d_5 -Nva**; B) **NO-5- d_3 -Nva**; C) **NO-4- d_2 -Nva**; D) **NO-Nva**, collected at $g_{eff} = 3.98$. Experimental conditions: Magnetic Field: 613.5 mT (A, B) and 613 mT (C, D); Microwave Frequency: 34.201 (A, D), 34.199 (B), and 34.202 (C) GHz; Temperature: 4.5 K (A) and 4.0 K (B, C, D). Contour levels are adjusted to the maximum of the ^2H signal with minimum at 50% of maximum.

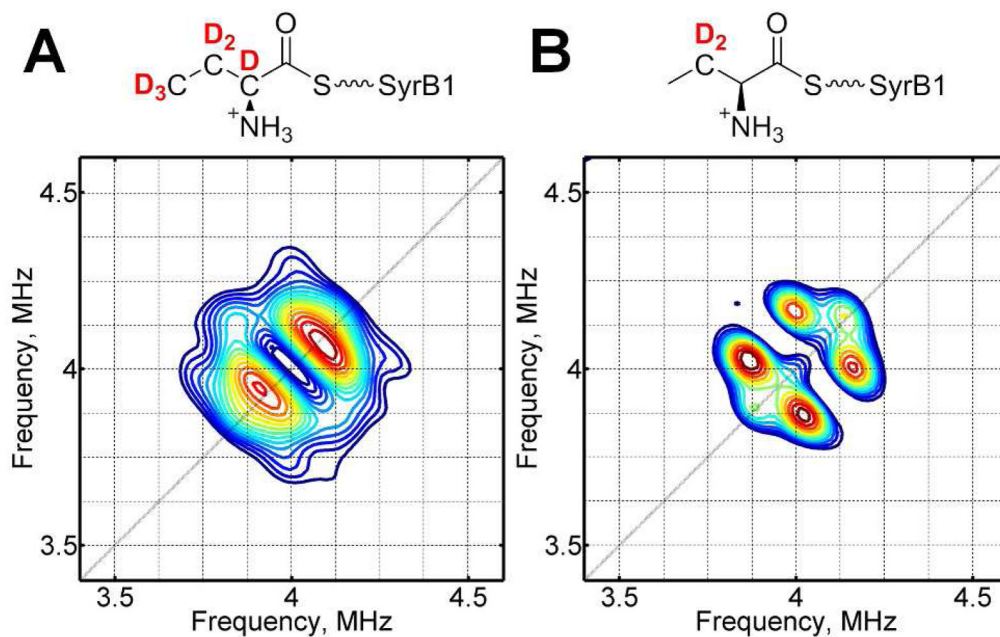


Figure 4. HYSCORE spectra and substrate chemical structures for A) **NO-per-d₆-Aba** and B) **NO-3-d₂-Aba**, collected at $g_{\text{eff}} = 3.98$. Experimental conditions: Magnetic Field: 611.9 mT (A), 613.5 mT (B); Microwave Frequency: 34.148 GHz (A), 34.200 GHz (B); Temperature: 4.65 K (A), 4.0 K (B). The contour levels are set as in Figure 3.

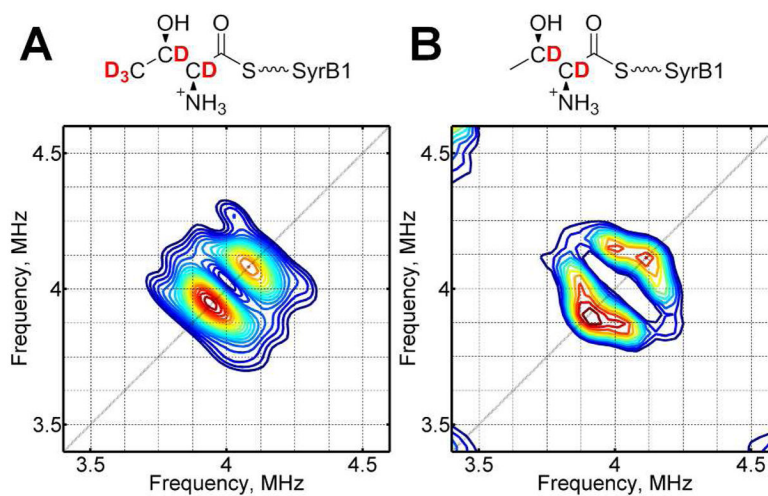


Figure 5. HYSCORE spectra and substrate chemical structures for A) NO-*per-d*₅-Thr; B) NO-2,3-*d*₂-Thr, collected at $g_{\text{eff}} = 3.98$. Experimental conditions: Magnetic Field: 613.6 mT (A), 613.5 mT (B); Microwave Frequency: 34.206 GHz (A) and 34.201 GHz (B); Temperature: 4.6 K (A) and 4.0 K (B). The contour levels are set as in Figure 3.

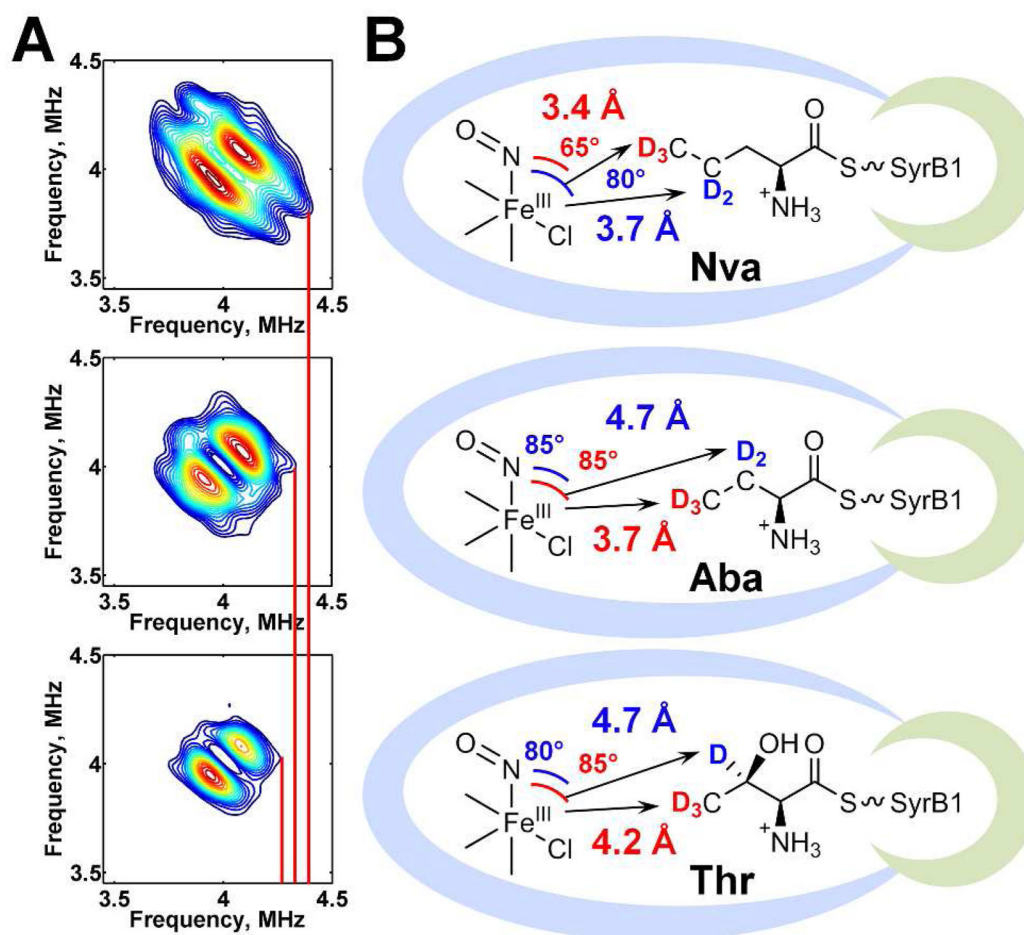


Figure 6.

A) Comparison of the ^2H -HYSCORE signals for **NO-4,5-*d*₅-Nva** (top), **NO-*per-d*₆-Aba** (center), and **NO-*per-d*₅-Thr** (bottom). Red, vertical bars have been added for ease of comparison. Spectra depicted were collected at $g_{\text{eff}} = 3.98$; experimental details are provided in the legends of Figures 3–5. B) SyrB2 active site models for substrates **Thr**, **Aba**, and **Nva**. Red labels indicate parameters for the methyl deuterons, whereas blue labels indicate the C3 deuterons in Aba and Thr, and the C4 deuterons in Nva.